Macro1 domain residue F156: A hallmark of SARS-CoV-2 de-MARylation specificity

Oney Ortega Granda, Karine Alvarez, Maria J Mate-Perez, Bruno Canard, François Ferron, Nadia Rabah

Macro1 domain residue F156: a hallmark of SARS-CoV-2 de-MARylation specificity

Oney Ortega Granda[a], Karine Alvarez[a], Maria J. Mate-Perez[a], Bruno Canard[a], François Ferron[a] and **Nadia Rabah[a,b*]**

[a] Aix Marseille Université, CNRS, AFMB UMR 7257, Marseille, France

[b] Previous affiliation : Université de Toulon, 83130 La Garde, France

***Corresponding author at :** Aix-Marseille Université, AFMB UMR 7257, 13288 Marseille Cedex 09, France.
E-mail address: nadia.rabah@univ-amu.fr (N. Rabah).

Abstract

SARS-CoV-2 is a large, enveloped and positive sense single stranded RNA virus. Its genome codes for 16 non-structural proteins. The largest protein of this complex is nsp3, that contains a well conserved *Macro1* domain. Viral *Macro* domains were shown to bind to mono-ADP-ribose (MAR) and poly-ADP-ribose (PAR) in their free form or conjugated to protein substrates. They carry ADP-ribose hydrolase activities implicated in the regulation of innate immunity. SARS-CoV-2 and SARS-CoV show widely different induction and handling of the host interferon response. Herein, we have conducted a mutational study on the key amino-acid residue F156 in SARS-CoV-2, pinpointed by bioinformatic and structural studies, and its cognate residue N157 in SARS-CoV. Our data suggest that the exchange of these residues slightly modifies ADP-ribose binding, but drastically impacts de-MARylation activity. Alanine substitutions at this position hampers PAR binding, abolishes MAR hydrolysis of SARS-CoV-2, and reduces by 70% this activity in the case of SARS-CoV.

Keywords: SARS-CoV-2, *Macro* domain, ADP-ribose, de-MARylation, ADP-ribose binding.

1. Introduction

Severe Acute Respiratory Syndrome (SARS) Coronavirus 2 (SARS-CoV-2) is the virus associated with the pandemic of coronavirus disease appeared in 2019 (COVID-19). SARS-CoV-2 is a member of the family *Coronaviridae*, the subfamily *Coronavirinae* and the subgenus sarbecoviruses (Pal et al., 2020). SARS-CoV-2 belongs to the β-coronavirus genus together with the previously identified SARS-CoV and MERS-CoV. All of these β-coronaviruses have been associated with human fatal diseases (L. Lu et al., 2020). SARS-CoV is the agent of SARS that caused 774 deaths and 8096 confirmed cases from 2002 to 2003 (Cherry, 2004). MERS-CoV emerged in 2012 spreading in the Middle East, with 2494 positive cases and 858 deaths (R. Lu et al., 2020). Although the mortality rate of SARS-CoV-2 (<2%) is low compared to that of SARS-CoV (9.6%) and MERS (35%), it spreads faster among humans. The mortality rate associated with SARS-CoV-2 infection can fluctuate considerably according to countries, patient age and health condition. Future epidemiological studies will shed light on the possible under or over estimation of the actual death rates (Abdelghany et al., 2021; Fani et al., 2020; Ioannidis, 2021; Pustake et al., 2022). Rapidly evolving vaccine strategies prove effective, but are constantly challenged by the emergence of new variants (Kim et al., 2021), advising the identification of viral druggable targets.

SARS-CoV-2 carries a positive-sense single-stranded RNA genome with a length of 29.9 kb (Wu et al., 2020), which codes for two large open reading frames (ORF1a and ORF1ab), the latter generated by a ribosomal frame-shift close to the ORF1a end. They lead to the production of two large polyproteins subsequently processed to 16 non-structural proteins nsp1 to 16. The last third of the genome encodes viral structural proteins: spike (S), envelope (E), membrane (M), nucleocapsid protein (N) and accessory proteins. The translation of this last part of the genome occurs *via* the production of individual subgenomic RNAs. Structural proteins ensure genomic packaging, encapsidation, virion formation and release (Kirtipal et al., 2020). Among the nsps, nsp3 is the largest multi-domain protein component of the replication/transcription complex (RTC), with an average molecular mass of about 200 kDa. Its architecture is however not absolutely conserved within CoV genera, due to duplication or deletion of some domains. In addition to two transmembrane regions (TM1 and TM2), eight regions remain conserved: the ubiquitin-like domain 1 (Ubl1), the hypervariable region (Glu-rich or acidic domain), a *Macro* domain (also named "X domain"), the ubiquitin-like domain 2 (Ubl2), the papain-like protease 2 ($PL2^{pro}$), a zinc-finger domain (ectodomain), the Y1 and CoV-Y domains of unknown functions (Lei et al., 2018). SARS-CoV and SARS-CoV-2 contains three tandem *Macro*- like domains (*Macro1* to 3). *Macro2* and *Macro3* interact with nucleic acids, whereas *Macro1* is involved in ADP-ribose binding and hydrolysis (Tan et al., 2009).

Macro domains are widely distributed among life kingdoms and are also coded by some (+) RNA viruses including *Togaviridae*, *Hepeviridae* and *Coronaviridae,* as mentioned above (Lei et al., 2018; Rack et al., 2016). These domains are able to bind various mono-ADP-ribose derivatives, including ADP-ribose 1" phosphate (Appr1p), O-acetyl-ADP-ribose, and PAR, in a free form or conjugated to protein or RNA substrates (Munnur et al., 2019; Munnur and Ahel, 2017). ADP-ribosylation is a ubiquitous post-translational modification affecting protein activity, interactions, ubiquitination and targeting of proteins for degradation. The reaction is driven by ADP-ribosyl transferases (ARTs), which promote the addition of one (MAR) or multiple/poly (PAR) ADP-ribose moieties onto charged amino acid residues, including Ser, Thr, Tyr, Arg, Lys, His, and Cys of target proteins. To date the ART superfamily comprises 23 families. One of the best characterized is the ARTD family, encompassing Poly-ADP-Ribosyl Polymerases (PARPs), which use nicotinamide adenine dinucleotide (NAD+) as a substrate (Lüscher et al., 2022). The PARP subfamily comprises ~17 members in humans. Their ADP-ribosylation activities are implicated in DNA repair, chromatin remodeling, transcriptional regulation, cell signalling, inflammation, and immune response (Brady et al., 2019). PARPs 1, 5a,7, 9, 10, 11, 12, 13 and 14 are involved in the regulation of innate immunity and provide an anti-viral effect *via*: (i) promoting viral proteins proteasome degradation; (ii) inhibiting translation machinery; (iii) inhibiting viral replication; (iv) stimulating the formation of stress granules; and (v) inducing interferon (IFN) signaling and interferon stimulated genes (ISGs) (Fehr et al., 2020; Hoch, 2021; Zhu et al., 2021; Zhu and Zheng, 2021).

ADP-ribosylation can be reversed by two enzyme families, namely: ADP-ribosyl hydrolases (ARHs) and *Macro* domains, including viral *Macro* domains (Egloff et al., 2006; Fehr et al., 2016; Li et al., 2016; Malet et al., 2006; McPherson et al., 2017). Hydrolysis activities are believed to counter the above-mentioned PARPs anti-viral effects. This assumption is supported by several *Macro* domain mutagenesis studies in which key residues implicated in ADP-ribose binding showed a reduction in virus replication and virulence of Hepatitis E virus (HEV), alphaviruses and several coronaviruses (Fehr et al., 2018). Hence, catalytic mutants of murine hepatitis virus (MHV) *Macro* domain failed to induce acute hepatitis in mice, and MHV growth was restricted in cells culture unless IFN receptor knockout cells were used, or PARPs inhibitors were added (Eriksson et al., 2008; Fehr et al., 2015; Grunewald et al., 2019). In HCoV-229, a *Macro* domain mutant virus becomes susceptible to IFN type I and II, and is unable to suppress the activation of ISGs (Kuri et al., 2011). In mouse adapted SARS-CoV, mutation of the *Macro* domain ADP-ribose binding pocket renders the virus more susceptible to cytokines, including IFN, TNF and IL-6, and protects mice from lethal infection (Fehr et al., 2016). Consistent with these data, SARS-CoV-2 infection alters PARP family gene expression and disrupts NAD+ biosynthesis (Heer et al., 2020). The accumulated data highlight

the importance of ADP-ribosylation in establishing infection, thus making *Macro* domain an interesting enzyme to understand virus-host interactions and their mitigations.

Amino-acid sequence comparison of nsp domains between SARS-CoV-2 and SARS-CoV reveals that the SARS-CoV-2 *Macro1* domain shares 71% identity with SARS-CoV, hence being the most divergent amongst nsps (Frick et al., 2020; Lin et al., 2020). The crystal structure of SARS-CoV-2 *Macro1* domain was solved in its free form (apo) and complexed to various ligands including 2-(N-morpholino) ethanesulfonic acid (MES), AMP and ADP-ribose. The reported structures follow the classical architecture described for *Macro* domains, with 7 β-sheets sandwiched between two layers of α-helixes (Alhammad et al., 2021; Frick et al., 2020; Lin et al., 2020; Michalska et al., 2020). Structural comparison studies between SARS-CoV-2 and SARS-CoV *Macro1* domains point to an unexpected difference at the heart of the *Macro1* domain active site: the F156 residue in SARS-CoV-2 corresponds to N157 residue in SARS-CoV. A divergence at this position suggests a significant change in the orientation of the ADP-ribose adenine group in the binding pocket between the *Macro1* domains of these two viruses, which might impact considerably ADP-ribose binding and/or hydrolysis kinetics, and might translate into difference on innate immune response observed against sarbecoviruses.

In the present study, we focus on SARS-CoV-2 F156 and SARS-CoV N157 *Macro1* domain residues. Through mutagenesis and functional studies, we evaluate the role of this particular residue on *Macro1* domain stability, ligand binding and ADP-ribose derivatives hydrolysis activity.

2. Materials and methods

2.1. Expression and Purification of the SARS-CoVs *Macro1* domain

The cDNA encoding nsp3 sequence of SARS-CoV (residues 182 to 355, GenBank #AY291315) and SARS-CoV-2 (residues 207 to 375, NCBI accession YP_009725299.1) were codon optimized and cloned into the pET28 vector (Novagen)-TWIST Bioscience. Mutagenesis was performed by PCR using Phusion High-Fidelity DNA Polymerase (NEB), as recommended by the manufacturer. Primers used for mutant generation are compiled in Table S1. The recombinant proteins were expressed in competent *E. coli* cells (C41 (DE3) plys). A detailed protocol on expression and purification of SARS-CoV was previously reported (Malet et al., 2006). The expression of SARS-CoV-2 recombinant protein was done in Turbo Broth medium (Cat#0104 AthernaES). The induction was carried with 50µM of IPTG ($O.D_{600\ nm}$ of 0.6) at 25°C for 12-14 hours. At the end of the incubation time, the cultures were centrifuged at 9000 rpm at 4°C for 30 min, and the pellets were

kept at -80°C until purification. Thawed bacterial pellet from *Macro1* domain of SARS-CoV-2 was resuspended in lysis buffer (50 mM Tris–HCl, pH 8, 150 mM NaCl, 20 mM MgSO4, 5% glycerol, 20 µg/mL DNase, 0.25mg/mL lysozyme and 1 mM PMSF) at 4°C for 1 hour. The cell lysate was sonicated and the supernatant was collected by centrifugation at 20,000 rpm for 25 min at 4°C. Immobilized metal affinity chromatography (IMAC) purification was performed using Ni-NTA column (GE Healthcare). The filtered supernatant was loaded into the column equilibrated with binding buffer (50 mM Tris–HCl, pH 8, 150 mM NaCl, 5% Glycerol and 10mM Imidazole). The column was then washed with 10 column volume of wash buffer (50 mM Tris–HCl, pH 8, 150mM NaCl, 5% Glycerol and 30 mM Imidazole) followed by a second wash with buffer supplemented with 1 M NaCl. Recombinant protein was eluted with elution buffer (50 mM Tris–HCl, pH 8, 150 mM NaCl, 5% Glycerol and 200 mM Imidazole). The fractions containing the purified protein were then pooled and dialysed against gel filtration (GF) buffer (50 mM Tris-HCl pH 8, 150 mM NaCl, 5% glycerol). In addition, a second purification step of size-exclusion chromatography was performed by injecting the protein into a Superdex 75 column (GE Healthcare) equilibrated with GF buffer. The eluted protein was concentrated in Vivaspin centrifugal concentrator (Sartotius) and stored at -80°C. The presence of the proteins in the fractions of interest was confirmed by western blot, using an anti-histidine antibody (Penta·His HRP, Quiagen). Mutants *Macro1* domains were expressed and purified following the same conditions as the corresponding wild-type recombinant proteins.

2.2. Poly (ADP-ribose) synthesis

PARylated protein was obtained through auto-ADP-ribosylation of human PARP1 (hPARP1) (Sigma SRP0192) in 300µL reaction volume, in the presence of 100 mM Tris pH 8, 10 mM $MgCl_2$, 2 mM DTT, 0.8 units hPARP1 and 250 µM NAD+. The reaction was carried at room temperature (RT) for 2 h under moderate agitation. PARylation was stopped by diluting the reaction in 20mL of dot blot buffer (10mM Tris pH 8,150 mM NaCl and 0.05 % Tween). The diluted reaction was directly used for the *Macro1* domain binding assay.

2.3. Binding assay

Binding affinity of ADP-ribose to SARS-CoV and SARS-CoV-2 was performed in Immobilon-PSQ PVDF membrane (MERCK Cat #ISEQ85R). The binding reactions were carried out by spotting serial dilutions (from 250 to 1.9 pmol) of recombinant *Macro1* domain proteins on nitrocellulose membrane using Minifold II dot blot apparatus (Schleicher & Schuell). Bovine serum albumin (BSA) was used as a negative control for the assay. The membrane was blocked with dot blot buffer supplemented with 4% skimmed milk, for 1 h, at RT. The blocked membrane was then incubated

with auto-ADP-ribosylated hPARP1 for 1h at RT under constant agitation. The unbound material was removed by three extensive washes with dot blot buffer. The primary antibody anti-PAR binding reagent (Sigma Cat #MABE1031) was used diluted 1:1500 in dot blot buffer with 1 % non-fat milk for 2 h, at RT. The secondary antibody, anti-rabbit IgG (Dako), was diluted 1/2000 in dot blot buffer and incubated with the membrane for 1 h, at RT. The membrane was washed three times in dot blot buffer after each anti-body. Immunoreactive signals were revealed using ECL reagent (Cat. # 170–5061, Bio-Rad) and visualized using Amersham™ ImageQuant™ 800 Immager system. Images were analyzed and quantified using ImageJ software (Schneider et al., 2012). Each experiment was repeated three times. Band's intensity was normalized to the total protein load.

2.4. Isothermal titration calorimetry (ITC)

ITC experiments were performed at 20°C using an Microcal iTC200 (Malvern Panalytical). Purified recombinant SARS-CoV and SARS-CoV-2 WT and mutant proteins were used at 150µM. The interaction was assessed in GF buffer, using 75 to 2000µM of ADP-ribose as injected ligand. Heat of dilution were measured by injecting the ligand into the protein solution. Titration curves were fitted with the MicroCal Origin software, assuming a one-site binding model, and enthalpy (ΔH), entropy changes (ΔS), dissociation equilibrium constants (K_D) and stoichiometry were extracted.

2.5. De-MARylation and de-PARylation assays

MARylated human PARP3 (hPARP3) was obtained by incubating 10µM of full length hPARP3 (Sigma SRP0194) in 25mM Tris pH 8, 100mM NaCl, 2 mM DTT, and 200µM NAD+ for 30 minutes at 30°C. De-MARylation activity was assessed by incubating 1µM of MARylated hPARP3 with 150 nM of recombinant *Macro1* domains at 37°C for a period of 0 to 30 min in the same buffer. The reaction was stopped by adding mPAGE™ 4X LDS Millipore sample buffer and heating at 95°C for 5 min. Autoribosylated hPARP3 protein without any *Macro1* domain served as negative control. Reactions were loaded on a 4 to 20% mPAGE bis-tris precasted gel (Millipore Cat#MP42G12). After migration, protein bands were transferred to nitrocellulose membrane (Amersham Cat#10600008) overnight at 4°C. The membranes were blocked with 4% non-fat milk in TBS-Tween buffer for 1 h. The primary antibody anti-MAR binding reagent (Sigma Cat # MABE1076) was used at a final dilution of 1/2500 in TBS-T with 1% non-fat milk for 1h. The membrane was then processed as described above in the dot blot binding assay. Quantification was done using ImageJ program. The results were normalized to the value of the negative control.

The de-PARylation activity was performed by incubating of 1 or 5uM of SARS-CoV and SARS-CoV-2 *Macro1* domain with 0.4 U of auto-PARylated hPARP1. The reactions were incubated for 1h at 37°C in the reaction buffer (100 mM Tris pH 8, 10 mM $MgCl_2$ and 2 mM DTT). After the

incubation time, the samples were subjected to the same process described above in de-MARylation activity. The primary antibody used to detect the PAR non-removed was anti-PAR binding reagent (Sigma Cat # MABE1076) diluted 1:1500 in TBS-T with 1% non-fat milk.

2.6. Protein stabilization assessment

2.6.1 Thermal shift assay (TSA)

Protein thermal shift assays were performed to determine the stability of SARS-CoV and SARS-CoV-2 *Macro1* domains proteins in presence of increases concentration of ADP-ribose (10µM to 1000µM). For that end, *Macro1* domain proteins were diluted in TSA buffer (20mM HEPES pH 8 and 150mM NaCl) to a final concentration of 2 µM. The test was performed in MicroAmp® Fast Optical 96-well reaction plates from Applied Biosystems. Protein thermal shift dye kit (Applied biosystems, Thermo Fisher Scientific) was used diluted in water, according to manufacturer's instructions. After mixing all components in the wells, the plate was sealed and put in the 7500 FastReal-Time PCR System (Applied Biosystems). The reaction was started by a first incubation step at 25°C for 2 min. The temperature was then increased with a ramp rate of 0.5°C per min to 95°C. Normalized melting curves were obtained with GraphPad Prism. The melting temperatures (Tm) were calculated from the inflection point of the melting curves.

2.6.2 HoTMuSiC tools

HoTMuSiC tools was used to predict the change in melting temperature (Tm) upon point mutations. For that purpose, the protein structure (SARS-CoV (PDB: 2FAV) and SARS-CoV-2 (PDB: 6WOJ) and the melting temperatures of the wild-type proteins (SARS-CoV (Tm=319KC) and SARS-CoV-2 (Tm=321K)), determined by TSA, were supplied.

3. Results and discussion

3.1. ADP-ribose binding coordination

The overall structure of the CoV *Macro1* domain consists of six α-helices and one seven-stranded β-sheet. The β-sheet (β1−β2−β7−β6−β3−β5−β4) is topped and bottomed by 3 α-helices (α1, α2, and α3 and α4, α5, and α6 respectively) thus delimiting a groove where the ligand binds (Fig 1). Comparative protein sequence analysis of SARS-CoV and SARS-CoV-2 *Macro1* domains (Fig 1A) reveals that most of the differences are located at the extremities of the domain namely the α1 helix and α1-β3 loop at the N-terminus, and the α6 helix at the C-terminus. Divergent residues between the two closely related viruses represent ~ 30 % of the sequence in accordance to previous reports (Frick et al., 2020; Lin et al., 2020). The structural basis of *Macro1* domain and ADP-ribose interactions have been characterized (Alhammad et al., 2021; Egloff et al., 2006; Frick et al., 2020;

Lin et al., 2020; Malet et al., 2009; Michalska et al., 2020). These studies pointed out that the ADP-ribose is partially buried in a chief hydrophobic cleft encompassing, in the case of SARS-CoV-2, the C-terminal end of β strands β3, β5, β6, β7 and two loops, β3-α2 and β6-α5 (Fig 1B and C). The cleft accommodating ADP-ribose creates four contact zones. The first contact zone forms a hydrophobic patch between the residues I23, V49, P125, V155 and F156 (all conserved except the latter), which interacts with adenine and points it toward the polar D at position 22. Residues interacting directly with ADP ribose are well conserved among various *Macro* domains. The residue D22 correspond to D23 in SARS-CoV (Fig 1E) and is present in other *Coronavirinae* members, alpha-like viruses and non-viral *Macro* domains (Allen et al., 2003; Cho et al., 2016; Fehr et al., 2018; Rack et al., 2020). Mutagenesis studies showed that these residues are crucial for ADP-ribosyl hydrolase and ADP-ribose-1'-phosphatase activities, and drastically impact viral replication and virulence (reviewed in (Fehr et al., 2018)). The second contact zone, a conserved glycine rich stretch (residues 46-48), accommodates the diphosphate moiety of ADP-ribose. Phosphate groups connecting adenosine moiety to the distal ribose interact with amide backbones of the main chain of residues within the loop β3−α2 and β6−α5 region. The α-phosphate forms hydrogen bonds with V49 and I131 while β-phosphate interacts with S128, G130 and F132 (Fig 1 D and E). Distal ribose fits tightly into the pocket formed by the nitrogen bonds between the amide group of G48, G46 and side chain of N40 and 1', 2' and 3'-hydroxyl groups of the ribose. The third contact zone implicates F132 and I131, which stabilize the proximal ribose. The forth contact zone, involving L126, together with A154 and D157, supports the distal ribose *via* water-hydrogen bonding (Alhammad et al., 2021; Frick et al., 2020; Lin et al., 2020; Michalska et al., 2020).

In SARS-CoV-2 the adenosine moiety is partially stacked by F156, which interacts edge-to-face with the aromatic ring system (Fig 1C and D). This residue corresponds to N157 in SARS-CoV (Fig 1E). The proximity of phenylalanine to the adenosine ring is only observed in SARS-CoV-2 among betacoronaviruses, even if other hydrophobic residues are present at that position. These data, in concert with previous 3D studies, might suggest a different alignment of ADP-ribose adenine group in the binding pocket of SARS-CoV-2.

3.2. Expression and Purification of recombinant *Macro1* domain proteins

In order to understand the influence of F156 on ADP-ribose binding and hydrolysis kinetics, we generated several substitutions leading to: (i) the exchange of F156 and N157 between *Macro1* domains of SARS-CoV-2 and SARS-CoV, respectively; (ii) the substitution of the target residues to alanine. To set a negative reference for comparison, mutations of D22 and D23, for SARS-CoV-2 and SARS-CoV, respectively, were also conducted. Recombinant *Macro1* domain proteins, with a

N-terminal 6 x His tag, of 172 amino acids (aa) and 168 aa, corresponding to SARS-CoV and SARS-CoV-2 respectively, were successfully expressed in *E. coli* (Fig 2A) and purified. Bands of about 20 kDa were observed in soluble purification fractions, and enriched throughout the purification process (Fig 2B). Despite being a 20.8 kDa protein, the *Macro1* domain of SARS-CoV-2 migrates slightly higher than that of SARS-CoV (20.9 kDa). The difference in the gel migration could be related to the difference in SDS adsorption of these two proteins. Besides, SARS-CoV-2 shows slight differences in purification buffer preferences as compared to SARS-CoV. First, significant amounts of SARS-CoV-2 were lost during the washing steps at the imidazole concentration used for SARS-CoV (60 mM). Thus, imidazole concentration was decreased to 30 mM. In contrast, salt concentration had to be increased to eliminate more tightly bound contaminants. After two purification steps (IMAC and gel filtration), proteins of interest were pure, as evidenced by SDS-PAGE after Coommassie blue staining (Fig 2C). Identities of WT SARS-CoV-2 and SARS-CoV recombinant *Macro1* domains were confirmed by Matrix Assisted Laser Desorption Ionization - Time of Flight (MALDI-TOF) mass spectrometry.

3.3. Assessment of CoV *Macro1* domains ADP-ribose binding

In order to accurately evaluate the characteristics of generated mutants, we started by setting the reference values for our WT *Macro1* domain proteins, in comparison to earlier reports. Hence, dot blot assay, previously reported (Egloff et al., 2006; Li et al., 2016; Malet et al., 2009), was first conducted using auto-PARylated hPARP1 and increasing amounts of WT *Macro1* domains (Fig 3A, middle panel), to asses PAR binding to WT *Macro1* domain proteins. Our results show that auto-PARylated hPARP1 binds to SARS-CoV and SARS-CoV-2 WT, and is detected using an anti-PAR antibody, in a concentration dependent manner (Fig.3A upper and middle panel). The quantified binding signal displays drastic differences, up to 75%, in PAR binding of SARS-CoV regarding to SARS-CoV-2 at various *Macro1* domain concentrations (Fig 3A, upper panel). N to F and F to N substitution in SARS-CoV and SARS-CoV-2, respectively do not impact PAR binding (Fig. 3A, lower panel). However, alanine substitutions at that position decrease PAR binding for both *Macro1* domains. Alanine replacements of the conserved aspartate residue (D23A and D22A for SARS-CoV and SARS-CoV-2, respectively) abrogate PAR binding (Fig. 3A, lower panel). PAR binding was previously reported for SARS-CoV (Egloff et al., 2006; Li et al., 2016) and SARS-COV-2 (Lin et al., 2020). Therefore, our data confirm preceding studies. Moreover, the differential in PAR binding capacity between SARS-CoV and SARS-CoV-2 illustrated in Fig 3A might suggest a lower PAR binding capacity of SARS-CoV-2 *Macro1* domain, compared to SARS-CoV, exemplified by the need of high concentrations of protein for the binding to occur. Differences in PAR binding were also noticed between SARS-CoV and alphaviruses (Egloff et al., 2006; Malet et al., 2009), the former being less prone to PAR binding compared to the latter. Knowing that PAR polymers can

vary in size and complexity (Han et al., 2011; Jankevicius et al., 2013), this might suggest that viruses have different PARylated targets.

Next, we determined the dissociation constants and thermodynamic parameters of ADP-ribose using ITC (Fig 3B, C, D and E). Previous studies investigated *Macro1* domain binding parameters towards ADP-ribose using ITC (Isothermal titration calorimetry) for various human pathogenic coronaviruses, including SARS-CoV and SARS-CoV-2. The reported K_D values vary between 10 and 24 μM for SARS-CoV, and 10 and 17 μM for SARS-CoV-2 (Cho et al., 2016; Egloff et al., 2006; Frick et al., 2020; Lin et al., 2020). The differences being due to slight variations in experimental protocols and constructs design. In our hands, computed K_D values for SARS-CoV and SARS-CoV-2 correspond to 5.9±2.9 μM and 11.5±5.7 μM, respectively (Table 1). As expected, the substitution of SARS-CoV-2 D22A and SARS-CoV D23A, tested as negative controls, had a detrimental effect on the ADP-ribose binding. The computed K_D for SARS-CoV D23A *Macro1* domain is 28.9±1.99 μM (Table 1). Unfortunately, in the case of SARS-CoV-2, binding kinetics could not be determined accurately because of precipitation issues, paralleling observations made for Chikungunya virus (CHIKV) (McPherson et al., 2017). To determine if the presence of F156 SARS-CoV-2 influences ADP-ribose binding into the pocket, K_D values were measured for the generated mutants. Substitution of F156N in SARS-CoV-2 and N157F in SARS-CoV slightly affects ADP-ribose binding affinities (Table1), with measured values of 6.17±1.66 μM for SARS-CoV N157F and 9.17±1.14 μM for SARS-CoV-2 F156N. Alanine replacement in SARS-CoV N157A led to a 2-fold increase in K_D (13.5±1.67 μM) compared to WT. Conversely, SARS-CoV-2 F156A substitution had minor consequences on ADP-ribose affinity, with a K_D of 9.8±3.43 μM. One can notice that enthalpy and entropy values are similar between SARS-CoV and SARS-CoV-2 WT proteins. The mutations of interest do not change drastically ΔH values, nevertheless leaning towards the disruption of energetically favourable noncovalent interactions. Besides, a slight trend of higher sensitivity for SARS-CoV-2 is observed, with up to 7-fold increase in ΔS value for SARS-CoV-2 F156A mutant; while overall stable for SARS-CoV mutant proteins (Table 1).

Table 1. Thermodynamic parameters for CoV *Macro1* domains determined by ITC.

CoV *Macro1* domain	K_D(μM)	ΔH(kcal/mol)	ΔS(cal/mol/deg)
SARS-CoV	5.9 ±2.4	-10.35 ± 0.21	-11.4
SARS-CoV-2	11.5 ± 5.7	-10.14 ± 0.13	-12.0
SARS-CoV-N157F	6.17 ± 1.66	-9.528 ± 0.17	-8.66
SARS-CoV-2 F156N	9.17 ± 1.14	-8.037 ± 0.2	-4.36
SARS-CoV N157A	13.5 ± 1.67	-9.352 ± 0.043	-9.63
SARS-CoV-2 F156A	9.8 ±3.43	-7.225 ± 0.37	-1.72
SARS-CoV D23A	28.9±1.99	-7.962±0.13	-6.39
SARS-CoV-2 D22A	ND		

K_D (dissociation constant), ΔH (enthalpy), ΔS (entropy), ND (Not determined)

Hence, even if SARS-CoV-2 F156N substitution drives the mutant toward SARS-CoV K_D value, single amino acid substitution is not sufficient, in this context, for a complete mimicking of SARS-CoV ADP-ribose binding characteristics. Interestingly, the simultaneous mutation of SARS-CoV-2 V24I/E25Q/F156N, mimicking MERS-CoV sequence, generated a *Macro1* domain with K_D value similar to that obtain for MERS-CoV (~3 µM) (Cho et al., 2016; Lin et al., 2021, 2020). More recently, while this paper was under revision, Tsika *et al* 2022, reported a study investigating the inhibitory effect of remdesivir metabolite GS-441524 on SARS-CoV, MERS-CoV and SARS-CoV-2 *Macro1* domains. They showed that F156 plays a key role with adjacent residues in the selective binding of GS-441524 to SARS-CoV-2 *Macro1* domain. In that context, they exchanged F and N residues between SARS-CoV-2 and MERS-CoV, showing that the substitution N154F in the later has no effect on ADP-ribose binding, similar to what we are reporting for SARS-CoV, possessing an N residue at that position. In their hands, the computed K_D value for SARS-CoV-2 F156N was 8.2 µM, in accordance with our study (Tsika et al., 2022). Previous mutational studies on CHIKV *Macro* domain and human *MacroD2*, targeting residues in the vicinity of the ADP-ribose binding pocket, including the residues corresponding to G48 and G130 in SARS-CoV-2 *Macro1* domain, disrupt the binding of ADP-ribose (Li et al., 2016; Malet et al., 2009; McPherson et al., 2017). In SARS-CoV-2 the proximity of F156 to D22 may impact the strength of hydrogen bonds formation, which could influence the side chain orientation of the ADP-ribose adenine base, as pointed out by the crystallographic studies. Structural determination of the *Macro1* domain in the apo form as well as in complex to various ligands highlighted that ADP-ribose binding pocket is dynamic and flexible, adapting to different ADP-ribose derivatives. The loop in between β7 and α6, harboring the F156 residue, participates to a hydrophobic patch accommodating the adenine portion of the ADP ribose. This patch, including A21, I23, V49, L126 and A154 (Fig1. D and E), facilitates hydrogen bonding between adenine's N6 atom and β-carboxyl group of D22 and insures the correct positioning of water molecules, crucial for catalysis (Alhammad et al., 2021; Correy et al., 2022; Lin et al., 2020; Michalska et al., 2020). Our results demonstrate that the swap of N and F between the two *Macro*1 domains or even a mutation to A at this position do not hamper ADP-ribose binding. However, alanine substitutions of the aspartate at positions 22 and 23 (in SARS-CoV-2 and SARS-CoV, respectively) hinder it. Hence, our data support the need of a synergistic effect between several molecular determinants for ADP-ribose positioning in the binding pocket.

3.4. Altered de-MARylation in CoV *Macro1* domains mutants

Viral *Macro* domains were shown to possess MAR and PAR hydrolytic activities leading to the removal of ADP-ribose derivatives from MARylated and PARylated proteins (Aguilar et al., 2022; Alhammad et al., 2021; Eckei et al., 2017; Jankevicius et al., 2013; Li et al., 2016; Rosenthal et al.,

2013). De-PARylation activity can be assessed by different ways including: (i) the use of radiolabeled [P^{32}] NAD^+ for PARPs auto-PARylation followed by the addition of the *Macro* domain containing protein and the quantification of PAR signal removal after SDS-PAGE migration; (ii) the use of cold auto-PARylated PARPs coupled to anti-PAR antibody detection following gel migration. In our hands, using the second method, de-PARylation activity was neither detected for SARS-CoV nor for SARS-CoV-2 *Macro1* domains (Fig 4A), at concentrations ranging from 0.1 to 10 µM. Our results are in accordance with previously published results on MacroD2 family, including viral *Macro* domains (Alhammad et al., 2021; Eckei et al., 2017; Jankevicius et al., 2013; Rosenthal et al., 2013). All these data underline the low PAR hydrolysis potential of viral *Macro* domains when compared to the Poly ADP-ribose glycohydrolase (PARG), the prototype of PAR hydrolytic enzymes, reversing the action of PARP enzymes in cells. Nevertheless, removal of radiolabelled PAR from auto-PARylated hPARP1, even if weak, was observed for Hepatitis E virus (HEV), Sindbis virus (SINV), Venezuelan equine encephalitis virus (VEEV) and SARS-CoV. In the case of HEV the activity was prompted by the presence of the helicase domain (Aguilar et al., 2022; Li et al., 2016). Furthermore, *Macro* domain's constructs used in different studies, cited above, varies slightly. The generated proteins present a shift of 3 to 8 amino acids at the NT and/or the CT. This might suggest that if this activity is indeed biologically relevant in the case of viral *Macro* domains, they may need additional molecular determinants to fulfill it.

To assess the effect of CoV *Macro1* domain mutation on protein de-MARylation, hPARP3 protein was used as a substrate in time course hydrolysis reactions (Fig 4 B and Fig. S1). hPARP3 is known to MARylate different substrates such as Tankyrase 1, the mitotic components NuMa, PARP1 and its self (Rodriguez-Vargas et al., 2019). Hence, MARylated hPARP3 was incubated in the presence of various CoV *Macro1* domain mutants at a 10:1 substrate-enzyme ration, otherwise the hydrolysis was too rapid. After the indicated time points, the reactions were subjected to mPAGE. Western blot using the anti-MAR regent allows de-MARylation assessment by the removal of the MAR signal (Fig 4B, upper panel). CoV *Macro1* domain load was controlled by mPAGE Coommassie blue staining (Fig 4B). Load controls for hPARP3, corresponding to Ponceau membrane staining are shown in (Fig 4B). Auto-MARylated hPARP3 without CoV *Macro1* domain served as a control for zero hydrolysis. Bands intensities were quantified and fitted in nonlinear regression curves (Fig 4B, lower panel). Both SARS-CoV-2 and SARS-CoV *Macro1* domains are able to remove almost completely MAR from hPARP3 within 30 minutes. Substrate decay is more important in SARS-CoV-2 (70-90% loss after 5-10 minutes) compared to SARS-CoV (30-70%) (Fig 4B, lower panel), in accordance with recently reported data (Alhammad et al., 2021). The effect of *Macro1* domain mutations on hPARP3 de-MARylation is intriguing. First, substitutions of the conserved D22 and D23 by alanine in SARS-CoV-2 and SARS-CoV, added to the study as negative controls for

hydrolysis activity, abolish totally the de-MARylation activity, corroborating the crucial role of this aspartic acid in the enzymatic activity. SARS-CoV-2 F156A mutant shows a complete loss in hydrolysis activity for the first 10 min. MAR hydrolysis hardly reaches 40% of WT value after 30 min. Alanine substitution in SARS-CoV has also a negative effect on de-MARylation, as observed for SARS-CoV N157A mutant. At 10 min the de-MARylation activity is reduced by 70% but not completely abolished. Intriguingly, SARS-CoV N157F and SARS-CoV-2 F156N mutants behaved as the mimicked parental *Macro1* domain. Hence, SARS-CoV N157F mutant shows an increased hydrolysis activity similar to that of SARS-CoV-2; whereas SARS-CoV-2 F156N MAR hydrolysis was impeded, reaching SARS-CoV values. It is interesting to note that in the study reported by Tsika et al, the MAR hydrolysis activity, tested on MARylated PARP10 at a 1:1 substrate-enzyme ratio, is slightly higher in SARS-CoV compared to SARS-CoV-2. However, the F156N mutation of the later led to the shift of the activity toward SARS-CoV and MERS-CoV values (Tsika et al., 2022), supporting the assumption that a F at that position has an impact on MAR-hydrolysis. The exact catalysis mechanism of *Macro* domains is still under debate, confronting two possible modes of action. One of which involves a water molecule, in the vicinity of the α-phosphate, acting as the nucleophile. The second relaying on the involvement of a nucleophilic residue, H45 in the case of SARA-CoV-2, mediating water molecule activation (Rack et al. 2016 and Correy et al. 2022). Considering these results as well as available structural data, one can hypothesize that the aromatic structure of phenylalanine in the hydrophobic cavity creates a stacking interaction with the adenine moiety, thus stabilizing the distal ribose, undergoing the nucleophilic attack, in the active site groove. This explanation might account for: (i) the improved activity observed for SARS-CoV-2 compared to SARS-CoV; and (ii) the detrimental effect on de-MARylation activity observed for SARS-CoV-2 F156A mutant. Still, the SARS-CoV N157A mutant does not lose completely the hydrolytic activity, suggesting that water molecule network might display significant differences between the two viruses.

3.5. Phenylalanine in the hydrophobic cavity stabilizes the *Macro1* domain groove.

To relate the observed activities to a possible modification of mutant proteins thermostability, CoV *Macro*1 domain sequences were subjected to the HoTMuSiC tool, to evaluate changes in melting temperature under point mutations, on the basis of its experimental 3D structure (Pucci et al., 2020). The obtained predictions, listed in Table 2, corroborate de-MARylation activity results. Thus, SARS-CoV-2 F156N has a negative ΔTm (-3.77) value, causing protein destabilization; while SARS-CoV N157F displays a ΔTm of +1.01, favoring thermostability. Alanine substitution at these positions impacts negatively protein stability with computed ΔTm values of - 3.39 and -0.49 for SARS-CoV-2 F156A and SARS-CoV N157A, respectively. These data endorse that F156, in SARS-CoV-2, and its corresponding N157 residue in SARS-CoV are key players in *Macro1* domain de-

MARylation activity. Mutation of the key aspartate residue to alanine, leading to a complete loss in hydrolytic activity, has also a deleterious impact on protein stability with a ΔTm of -2.35 and -1.93 for SARS-CoV-2 D22A and SARS-CoV D23A *Macro1* domain, respectively (Table 2).

Subsequently, to verify experimentally the impact of the studied mutations on *Macro*1 domain stability, WT and mutant proteins were subjected to thermal shift assay in presence of increases concentrations of ADP-ribose. The data is complied in the Fig 5. The experimental ΔTm reported in the table 2 correspond to the values measured at the highest ADP-ribose concentrations in Fig 5. Thus, the F156N substitution in SARS-CoV-2 decreases the ΔTm (-1.1K) compared to the WT. In the case of N157F in SARS-CoV, no significant change is observed. However, the ΔTm are highly impaired in all alanine mutants. F156A exhibits a significant decay of ΔTm~(-4K) in SARS-CoV-2 and ΔTm (-3,4K) in the case of N157A in SARS-CoV. As expected, substitutions of aspartic acid by alanine drastically disrupted *Macro1* domain stability, supporting the importance of this residue in ADP-ribose stabilization through hydrogen bonding (Correy et al., 2022). In spite of the little differences between ΔTm absolute values, the experimental data corroborate the HoTMuSiC predicted values.

Table 2. Changes in melting temperature for CoV *Macro1* domain mutants determined by HoTMuSiC and TSA.

CoV *Macro1* domain mutants	HoTMuSiC ΔTm (K)	Experimental ΔTm (K)
SARS-CoV-N157F	1.01	-0.3
SARS-CoV-2 F156N	-3.77	-1.1
SARS-CoV N157A	-0.39	-3.4
SARS-CoV-2 F156A	-3.39	-3.9
SARS-CoV D23A	-2.35	-4.5
SARS-CoV-2 D22A	-1.93	-5.1

ΔTm (melting temperature), K (Kelvin)

Despite a high similarity in terms of sequence and function among viral *Macro* domains, notable differences in their affinity for ADP-ribose and catalytic activity indeed exist, affecting the state of ADP-ribosylation substrates in the cell. Multiple studies link viral *Macro* domain ADP-ribose hydrolase activity to viral pathogenesis. Mutations targeting residues D23, N41, H46 and G131 in SARS-CoV (Fig 1E) and equivalent positions in other RNA viruses, were shown to be deleterious for ADP-ribose binding/hydrolysis activity, PARP activation, and viral virulence (Egloff et al., 2006; Grunewald et al., 2019; Lin et al., 2020; McPherson et al., 2017; Michalska et al., 2020). As an example, in the case of SARS-CoV N41 catalytic residue, the *Macro1* domain mutant N41A is devoid of MAR-hydrolase activity and elicits more significant IFN, ISGs and pro-inflammatory cytokines production than the wild type virus in infected mice (Fehr et al., 2016). In MHV,

mutation of the D residue (D16, numbered D1329 in ORF1a polyprotein) to A has a severe impact on virus replication and the mutant virus is defective in blocking IFN production (Grunewald et al., 2019; Jankevicius et al., 2013). The phenomenon is emphasized when this mutation is combined to the substitution N30A (numbered N1347A in ORF1a polyprotein). The latter corresponds to N40 in SARS-CoV-2, involved in distal ribose interaction, through hydrogen bound formation with the C3" hydroxyl of the ADP-ribose (Correy et al., 2022; Voth et al., 2021). A recent study reports the impact of SARS-CoV-2 N40 mutation on PARP9 activation and IFN signaling (Russo et al., 2021), highlighting the importance of this residue in immune escape *via* STAT signaling. The substitution of D10A, G32E and G112E in CHIKV *Macro* domain, corresponding to D22, G48 and G130 in SARS-CoV-2 *Macro1* domain, decreased the MAR-hydrolase activity. The mutants were unable to produce viable CHIKV (McPherson et al., 2017). Also, the D22V mutation in SARS-CoV-2 and D23A in SARS-CoV impedes its activity, stressing the crucial role of this residues in the hydrolysis activity (Fehr et al., 2016; Rack et al., 2020). Former studies reported *Macro* domains with reduced affinity for ADP-ribose retaining high MAR hydrolase activity or *vice versa*. Yet, studies on CHIKV *Macro* domain showed that Y114 substitution, corresponding to F132 in SARS-CoV-2 and situated in the stretch accommodating the diphosphate moiety of ADP-ribose, impaired MAR hydrolysis activity but not ADP-ribose binding, hampering viral replication (McPherson et al., 2017). In accordance with these results, mutagenesis of V133 and Y114 residues in other *Macro* domains, corresponding to I131 and F132 and in SARS-CoV-2, also disrupted the hydrolysis activities without affecting ADP-ribose binding (Jankevicius et al., 2013; Zhang et al., 2015). Moreover, substitution of conserved Y126 by F in *E. coli Macro* domain containing YmdB protein, corresponding to F132 in SARS-CoV-2, showed a higher hydrolysis activity, highlighting the importance of the phenyl group for the catalytic activity (Zhang et al., 2015). Interestingly, F132L replacement in SARS-CoV-2 impedes MAR hydrolysis activity, as in CHIKV, but F156L substitution did not show a drastic effect on ADP-ribose hydrolysis from auto-ribosylated PARP14 WWE-CAT after 1 hour of reaction (Rack et al., 2020). In our hands, when the incubation is done for one hour, no differences are observed, since all the ADP-ribose is quickly removed.

The change of Asparagine by phenylalanine in SARS-CoV-2 seems to enhance π-π stacking interactions at the ADP-ribose site due to the flexibility of the aromatic side chain of this residue. Recently, a number of identified compounds, targeting SARS-CoV-2 *Macro1* domain, were shown to interact closely with F156 through π-stacking (Correy et al., 2022; Roy et al., 2022; Schuller et al., 2021). Structural data highlighted the importance of F156N substitution in SARS-CoV-2 and our experimental data brought some explanations on how this substitution is impacting the hydrolysis activity of SARS-CoV and SARS-CoV-2 *Macro1* domains. Hence, the phenylalanine is a key residue for stabilizing the protein, as well as an important residue to consider for the antiviral

design (Ni et al., 2021; Tsika et al., 2022). It is pointing out the importance of the hydrophobic patch at that position in SARS-CoV-2, and highlights the fact that many questions remain regarding the role of non-conserved and/or non-catalytic residues.

Thus, understanding how this residue and corresponding residues in other CoVs impact activity and ultimately infection of the virus could contribute significantly to drug design of pan-coronavirus *Macro1* domain inhibitors.

4. Conclusions

Finally, the importance of F156 residue in SARS-CoV-2 for MAR hydrolysis and ADP-ribose binding was investigated experimentally. Mutational analysis conducted in the present paper shed some light on functional differences in terms of ADP-ribose binding affinities and MAR hydrolysis activities of SARS-CoV and of SARS-CoV-2 *Macro1* domains, boarding our knowledge on *Macro* domains function, a pre-requisite for anti-viral drug design.

5. Acknowledgement

We would like to thank the Fondation Méditerranée Infection and the Innovative Medicines Initiative 2 Joint Undertaking (JU) under grant agreement No 101005077 (IMI-CARE) for financial support. The authors would like to thank Bhawna SAMA for her critical reading of the manuscript.

6. Declaration of competing interest

The authors declare that they have no known competing financial interests or personal relationships that could have appeared to influence the work reported in this paper.

7. Credit authorship contribution statement

Oney Ortega Granda: Conceptualization, Investigation, Methodology, Software, Writing – Original Draft, Review & Editing. **Karine Alvarez:** Resources, Writing – Review & Editing. **Maria J. Mate-Perez:** Methodology, Writing – Review & Editing. **Bruno Canard:** Resources, Writing – Review & Editing. **François Ferron:** Conceptualization, Investigation, Resources, Software, Writing – Review & Editing. **Nadia Rabah:** Conceptualization, Investigation, Methodology, Project Administration, Resources, Software, Writing – Original Draft, Writing – Review & Editing.

8. Figure captions

Fig 1. Sequence alignment and structure superposition of SARS-CoV with SARS-CoV-2 *Macro1* domain proteins. (A) SeaView comparison of SARS-CoV and SARS-CoV-2 *Macro1* domains. Secondary-structure elements are represented above the alignment, indicating the number and position of β-sheets and α-helices. Residues with strict identity are marked in red box, whereas residues considered as highly similar are dyed in red and framed in blue. Sequences and 3D structure of SARS-CoV (PDB: 2FAV) and SARS-CoV-2 (PDB: 6WOJ) *Macro1* domains were extracted from PDB. Superposition and the alignment were made with Chimera (Pettersen et al., 2004) and visualized using the ESPript (Robert and Gouet, 2014). (B) SARS-CoV (blue) and SARS-CoV-2 (green) structure superposition with ADP-ribose. The secondary structures are labeled and ADP-ribose molecule is shown in yellow sticks with oxygens (red), nitrogens (blue) and water (red spheres). (C) An expanded close-up view of the ADP-ribose binding groove superposition highlights the amino acids with major divergence N157 in SARS-CoV and F156 in SARS-CoV-2. ADP-ribose coordinates with their interacting amino acids in the binding cleft of SARS-CoV-2 (D) and SARS-CoV (E). Chemical structure of ADP-ribose and corresponding amino acids are exposed according to stick and balls model. Interaction of covalent bonds of ADP-ribose are shown in purple and of amino acid residues in brown. Hydrogen bonds formed between residues and ligand are represented as green dashed lines with the bond length as numeric numbers. Surrounding residues, in the hydrophobic pocket, in contact with ADP-ribose, are displayed as red eyelash symbols. Diagrams were generated by using LigPlot+ (Laskowski and Swindells, 2011).

Fig 2. Expression and purification of recombinant SARS-CoV and SARS-CoV-2 *Macro1* domains. (A) Western blot probing the expressed recombinant proteins insoluble (IF) and soluble (SF) expression fraction. (B) SDS-PAGE of bacterially expressed SARS-CoV-2 *Macro1* domain following IMAC purification (E1-9: elution fractions; W: wash; UB: unbound material). (C) SDS-PAGE of SARS-CoV-2 *Macro1* domain elution fraction (GF1 to 5) after Gel filtration chromatography.

Fig 3. ADP-ribose binding to SARS-CoV and SARS-CoV-2 recombinant *Macro1* domains. (A) Upper Panel: Dot blot binding signal quantification of WT proteins using ImageJ software. Average and standard deviation were computed using the GraphPad Prism program. Middle and lower panels: Dot blot auto-PARylated hPARP1 binding to SARS-CoV and SARS-CoV-2 WT and mutant recombinant proteins. BSA is used as a negative control for PAR binding. (B, C, D and E) ITC analysis of SARS-CoV and SARS-CoV-2 WT and mutant proteins titrated with ADP-ribose. Top panels show the heat variation upon injection as a function of time. Bottom panels represent the curve of integrated raw data as a function of the molar concentration of injectant.

Fig 4. de-PARylation and de-MARylation by CoV *Macro1* domains. (A) Western blot of auto-PARylated hPARP1 with SARS-CoV and SARS-CoV-2 *Macro1* domains. (B, upper panel) Western blot with anti-MAR binding reagent, assessing MAR hydrolysis from hPARP3. Ponceau red staining of WB membrane for hPARP3 protein load control. mPAGE Coommassie blue staining for *Macro1* domain protein load control. The results are representative of three independent experiments. (B, lower pannel) Bands intensity were quantified using ImageJ software and fitted to a nonlinear regression curve. Error bars indicate standard deviation.

Fig 5. Effect of mutation on the thermal stability of SARS-CoV and SARS-CoV-2 *Macro1* domains. Melting temperature profiles of SARS-CoV, SARS-CoV-2 WT and mutant *Macro1* domains in presence of increasing contractions of ADP-ribose. See Material and Methods for experimental details. Error bars indicate standard deviation.

685 # References

Abdelghany, T.M., Ganash, M., Bakri, M.M., Qanash, H., Al-Rajhi, A.M.H., Elhussieny, N.I., 2021. SARS-CoV-2, the other face to SARS-CoV and MERS-CoV: Future predictions. Biomedical Journal 44, 86–93. https://doi.org/10.1016/j.bj.2020.10.008

Aguilar, E.G., Paniccia, G., Adura, C., Singer, Z.S., Ashbrook, A.W., Razooky, B.S., Rice, C.M., MacDonald, M.R., 2022. Sindbis Macrodomain Poly-ADP-Ribose Hydrolase Activity Is Important for Viral RNA Synthesis. J Virol 96, e01516-21. https://doi.org/10.1128/jvi.01516-21

Alhammad, Y.M.O., Kashipathy, M.M., Roy, A., Gagné, J.-P., McDonald, P., Gao, P., Nonfoux, L., Battaile, K.P., Johnson, D.K., Holmstrom, E.D., Poirier, G.G., Lovell, S., Fehr, A.R., 2021. The SARS-CoV-2 Conserved Macrodomain Is a Mono-ADP-Ribosylhydrolase. J Virol 95, e01969-20. https://doi.org/10.1128/JVI.01969-20

Allen, M.D., Buckle, A.M., Cordell, S.C., Löwe, J., Bycroft, M., 2003. The Crystal Structure of AF1521 a Protein from Archaeoglobus fulgidus with Homology to the Non-histone Domain of MacroH2A. Journal of Molecular Biology 330, 503–511. https://doi.org/10.1016/S0022-2836(03)00473-X

Atasheva, S., Akhrymuk, M., Frolova, E.I., Frolov, I., 2012. New PARP Gene with an Anti-Alphavirus Function. Journal of Virology 86, 8147–8160. https://doi.org/10.1128/JVI.00733-12

Brady, P.N., Goel, A., Johnson, M.A., 2019. Poly(ADP-Ribose) Polymerases in Host-Pathogen Interactions, Inflammation, and Immunity. Microbiol Mol Biol Rev 83, e00038-18. https://doi.org/10.1128/MMBR.00038-18

Cherry, James.D., 2004. The chronology of the 2002–2003 SARS mini pandemic. Paediatric Respiratory Reviews 5, 262–269. https://doi.org/10.1016/j.prrv.2004.07.009

Cho, C.-C., Lin, M.-H., Chuang, C.-Y., Hsu, C.-H., 2016. Macro Domain from Middle East Respiratory Syndrome Coronavirus (MERS-CoV) Is an Efficient ADP-ribose Binding Module: CRYSTAL STRUCTURE AND BIOCHEMICAL STUDIES. J. Biol. Chem. 291, 4894–4902. https://doi.org/10.1074/jbc.M115.700542

Correy, G.J., Kneller, D.W., Phillips, G., Pant, S., Russi, S., Cohen, A.E., Meigs, G., Holton, J.M., Gahbauer, S., Thompson, M.C., Ashworth, A., Coates, L., Kovalevsky, A., Meilleur, F., Fraser, J.S., 2022. The mechanisms of catalysis and ligand binding for the SARS-CoV-2 NSP3 macrodomain from neutron and x-ray diffraction at room temperature. Sci. Adv. 8, eabo5083. https://doi.org/10.1126/sciadv.abo5083

Eckei, L., Krieg, S., Bütepage, M., Lehmann, A., Gross, A., Lippok, B., Grimm, A.R., Kümmerer, B.M., Rossetti, G., Lüscher, B., Verheugd, P., 2017. The conserved macrodomains of the non-structural proteins of Chikungunya virus and other pathogenic positive strand RNA viruses function as mono-ADP-ribosylhydrolases. Sci Rep 7, 41746. https://doi.org/10.1038/srep41746

Egloff, M.-P., Malet, H., Putics, A., Heinonen, M., Dutartre, H., Frangeul, A., Gruez, A., Campanacci, V., Cambillau, C., Ziebuhr, J., Ahola, T., Canard, B., 2006. Structural and Functional Basis for ADP-Ribose and Poly(ADP-Ribose) Binding by Viral Macro Domains. Journal of Virology 80, 8493–8502. https://doi.org/10.1128/JVI.00713-06

Eriksson, K.K., Cervantes-Barragan, L., Ludewig, B., Thiel, V., 2008. Mouse Hepatitis Virus Liver Pathology Is Dependent on ADP-Ribose-1’’-Phosphatase, a Viral Function Conserved in the Alpha-Like Supergroup. Journal of Virology 82, 12325–12334. https://doi.org/10.1128/JVI.02082-08

Fani, M., Teimoori, A., Ghafari, S., 2020. Comparison of the COVID-2019 (SARS-CoV-2) pathogenesis with SARS-CoV and MERS-CoV infections. Future Virology 15, 317–323. https://doi.org/10.2217/fvl-2020-0050

Fehr, A.R., Athmer, J., Channappanavar, R., Phillips, J.M., Meyerholz, D.K., Perlman, S., 2015. The nsp3 Macrodomain Promotes Virulence in Mice with Coronavirus-Induced Encephalitis. J Virol 89, 1523–1536. https://doi.org/10.1128/JVI.02596-14

Fehr, A.R., Channappanavar, R., Jankevicius, G., Fett, C., Zhao, J., Athmer, J., Meyerholz, D.K., Ahel, I., Perlman, S., 2016. The Conserved Coronavirus Macrodomain Promotes Virulence and Suppresses the Innate Immune Response during Severe Acute Respiratory Syndrome Coronavirus Infection. mBio 7, e01721-16. https://doi.org/10.1128/mBio.01721-16

Fehr, A.R., Jankevicius, G., Ahel, I., Perlman, S., 2018. Viral Macrodomains: Unique Mediators of Viral Replication and Pathogenesis. Trends in Microbiology 26, 598–610. https://doi.org/10.1016/j.tim.2017.11.011

Fehr, A.R., Singh, S.A., Kerr, C.M., Mukai, S., Higashi, H., Aikawa, M., 2020. The impact of PARPs and ADP-ribosylation on inflammation and host–pathogen interactions. Genes Dev. 34, 341–359. https://doi.org/10.1101/gad.334425.119

Frick, D.N., Virdi, R.S., Vuksanovic, N., Dahal, N., Silvaggi, N.R., 2020. Molecular Basis for ADP-Ribose Binding to the Mac1 Domain of SARS-CoV-2 nsp3. Biochemistry 59, 2608–2615. https://doi.org/10.1021/acs.biochem.0c00309

Grunewald, M.E., Chen, Y., Kuny, C., Maejima, T., Lease, R., Ferraris, D., Aikawa, M., Sullivan, C.S., Perlman, S., Fehr, A.R., 2019. The coronavirus macrodomain is required to prevent PARP-mediated inhibition of virus replication and enhancement of IFN expression. PLOS Pathogens 15, e1007756. https://doi.org/10.1371/journal.ppat.1007756

Han, W., Li, X., Fu, X., 2011. The macro domain protein family: Structure, functions, and their potential therapeutic implications. Mutation Research/Reviews in Mutation Research 727, 86–103. https://doi.org/10.1016/j.mrrev.2011.03.001

Heer, C.D., Sanderson, D.J., Voth, L.S., Alhammad, Y.M.O., Schmidt, M.S., Trammell, S.A.J., Perlman, S., Cohen, M.S., Fehr, A.R., Brenner, C., 2020. Coronavirus infection and PARP expression dysregulate the NAD metabolome: An actionable component of innate immunity. J Biol Chem 295, 17986–17996. https://doi.org/10.1074/jbc.RA120.015138

Hoch, N.C., 2021. Host ADP-ribosylation and the SARS-CoV-2 macrodomain. Biochemical Society Transactions 49, 1711–1721. https://doi.org/10.1042/BST20201212

Ioannidis, J.P.A., 2021. Over- and under-estimation of COVID-19 deaths. Eur J Epidemiol 36, 581–588. https://doi.org/10.1007/s10654-021-00787-9

Jankevicius, G., Hassler, M., Golia, B., Rybin, V., Zacharias, M., Timinszky, G., Ladurner, A.G., 2013. A family of macrodomain proteins reverses cellular mono-ADP-ribosylation. Nat Struct Mol Biol 20, 508–514. https://doi.org/10.1038/nsmb.2523

Kim, J.H., Marks, F., Clemens, J.D., 2021. Looking beyond COVID-19 vaccine phase 3 trials. Nat Med 27, 205–211. https://doi.org/10.1038/s41591-021-01230-y

Kirtipal, N., Bharadwaj, S., Kang, S.G., 2020. From SARS to SARS-CoV-2, insights on structure, pathogenicity and immunity aspects of pandemic human coronaviruses. Infect Genet Evol 85, 104502. https://doi.org/10.1016/j.meegid.2020.104502

Kuri, T., Eriksson, K.K., Putics, A., Züst, R., Snijder, E.J., Davidson, A.D., Siddell, S.G., Thiel, V., Ziebuhr, J., Weber, F., 2011. The ADP-ribose-1″-monophosphatase domains of severe acute respiratory syndrome coronavirus and human coronavirus 229E mediate resistance to antiviral interferon responses. Journal of General Virology 92, 1899–1905. https://doi.org/10.1099/vir.0.031856-0

Laskowski, R.A., Swindells, M.B., 2011. LigPlot+: Multiple Ligand–Protein Interaction Diagrams for Drug Discovery. J. Chem. Inf. Model. 51, 2778–2786. https://doi.org/10.1021/ci200227u

Lei, J., Kusov, Y., Hilgenfeld, R., 2018. Nsp3 of coronaviruses: Structures and functions of a large multi-domain protein. Antiviral Research 149, 58–74. https://doi.org/10.1016/j.antiviral.2017.11.001

Li, C., Debing, Y., Jankevicius, G., Neyts, J., Ahel, I., Coutard, B., Canard, B., 2016. Viral Macro Domains Reverse Protein ADP-Ribosylation. J. Virol. 90, 8478. https://doi.org/10.1128/JVI.00705-16

Lin, M.-H., Chang, S.-C., Chiu, Y.-C., Jiang, B.-C., Wu, T.-H., Hsu, C.-H., 2020. Structural, Biophysical, and Biochemical Elucidation of the SARS-CoV-2 Nonstructural Protein 3 Macro Domain. ACS Infect. Dis. 6, 2970–2978. https://doi.org/10.1021/acsinfecdis.0c00441

Lin, M.-H., Cho, C.-C., Chiu, Y.-C., Chien, C.-Y., Huang, Y.-P., Chang, C.-F., Hsu, C.-H., 2021. Elucidating the tunability of binding behavior for the MERS-CoV macro domain with NAD metabolites. Commun Biol 4, 123. https://doi.org/10.1038/s42003-020-01633-6

Lu, L., Zhong, W., Bian, Z., Li, Z., Zhang, K., Liang, B., Zhong, Y., Hu, M., Lin, L., Liu, J., Lin, X., Huang, Y., Jiang, J., Yang, X., Zhang, X., Huang, Z., 2020. A comparison of mortality-related risk factors of COVID-19, SARS, and MERS: A systematic review and meta-analysis. Journal of Infection 81, e18–e25. https://doi.org/10.1016/j.jinf.2020.07.002

Lu, R., Zhao, X., Li, J., Niu, P., Yang, B., Wu, H., Wang, W., Song, H., Huang, B., Zhu, N., Bi, Y., Ma, X., Zhan, F., Wang, L., Hu, T., Zhou, H., Hu, Z., Zhou, W., Zhao, L., Chen, J., Meng, Y., Wang, J., Lin, Y., Yuan, J., Xie, Z., Ma, J., Liu, W.J., Wang, D., Xu, W., Holmes, E.C., Gao, G.F., Wu, G., Chen, W., Shi, W., Tan, W., 2020. Genomic characterisation and epidemiology of 2019 novel coronavirus: implications for virus origins and receptor binding. The Lancet 395, 565–574. https://doi.org/10.1016/S0140-6736(20)30251-8

Lüscher, B., Ahel, I., Altmeyer, M., Ashworth, A., Bai, P., Chang, P., Cohen, M., Corda, D., Dantzer, F., Daugherty, M.D., Dawson, T.M., Dawson, V.L., Deindl, S., Fehr, A.R., Feijs, K.L.H., Filippov, D.V., Gagné, J., Grimaldi, G., Guettler, S., Hoch, N.C., Hottiger, M.O., Korn, P., Kraus, W.L., Ladurner, A., Lehtiö, L., Leung, A.K.L., Lord, C.J., Mangerich, A., Matic, I., Matthews, J., Moldovan, G., Moss, J., Natoli, G., Nielsen, M.L., Niepel, M., Nolte, F., Pascal, J., Paschal, B.M., Pawłowski, K., Poirier, G.G., Smith, S., Timinszky, G., Wang, Z., Yélamos, J., Yu, X., Zaja, R., Ziegler, M., 2022. ADP-ribosyltransferases, an update on function and nomenclature. The FEBS Journal 289, 7399–7410. https://doi.org/10.1111/febs.16142

Malet, H., Coutard, B., Jamal, S., Dutartre, H., Papageorgiou, N., Neuvonen, M., Ahola, T., Forrester, N., Gould, E.A., Lafitte, D., Ferron, F., Lescar, J., Gorbalenya, A.E., de Lamballerie, X., Canard, B., 2009. The Crystal Structures of Chikungunya and Venezuelan Equine Encephalitis Virus nsP3 Macro Domains Define a Conserved Adenosine Binding Pocket. Journal of Virology 83, 6534–6545. https://doi.org/10.1128/JVI.00189-09

Malet, H., Dalle, K., Brémond, N., Tocque, F., Blangy, S., Campanacci, V., Coutard, B., Grisel, S., Lichière, J., Lantez, V., Cambillau, C., Canard, B., Egloff, M.-P., 2006. Expression, purification and crystallization of the SARS-CoV *macro* domain. Acta Crystallogr F Struct Biol Cryst Commun 62, 405–408. https://doi.org/10.1107/S1744309106009274

McPherson, R.L., Abraham, R., Sreekumar, E., Ong, S.-E., Cheng, S.-J., Baxter, V.K., Kistemaker, H.A.V., Filippov, D.V., Griffin, D.E., Leung, A.K.L., 2017. ADP-ribosylhydrolase activity of Chikungunya virus macrodomain is critical for virus replication and virulence. Proc Natl Acad Sci USA 114, 1666–1671. https://doi.org/10.1073/pnas.1621485114

Michalska, K., Kim, Y., Jedrzejczak, R., Maltseva, N.I., Stols, L., Endres, M., Joachimiak, A., 2020. Crystal structures of SARS-CoV-2 ADP-ribose phosphatase: from the apo form to ligand complexes. IUCrJ 7, 814–824. https://doi.org/10.1107/S2052252520009653

Munnur, D., Ahel, I., 2017. Reversible mono-ADP-ribosylation of DNA breaks. FEBS J 284, 4002–4016. https://doi.org/10.1111/febs.14297

Munnur, D., Bartlett, E., Mikolčević, P., Kirby, I.T., Rack, J.G.M., Mikoč, A., Cohen, M.S., Ahel, I., 2019. Reversible ADP-ribosylation of RNA. Nucleic Acids Research 47, 5658–5669. https://doi.org/10.1093/nar/gkz305

Ni, X., Schröder, M., Olieric, V., Sharpe, M.E., Hernandez-Olmos, V., Proschak, E., Merk, D., Knapp, S., Chaikuad, A., 2021. Structural Insights into Plasticity and Discovery of Remdesivir Metabolite GS-441524 Binding in SARS-CoV-2 Macrodomain. ACS Med. Chem. Lett. 12, 603–609. https://doi.org/10.1021/acsmedchemlett.0c00684

Pal, M., Berhanu, G., Desalegn, C., Kandi, V., 2020. Severe Acute Respiratory Syndrome Coronavirus-2 (SARS-CoV-2): An Update. Cureus. https://doi.org/10.7759/cureus.7423

Pettersen, E.F., Goddard, T.D., Huang, C.C., Couch, G.S., Greenblatt, D.M., Meng, E.C., Ferrin, T.E., 2004. UCSF Chimera?A visualization system for exploratory research and analysis. J. Comput. Chem. 25, 1605–1612. https://doi.org/10.1002/jcc.20084

Pucci, F., Kwasigroch, J.M., Rooman, M., 2020. Protein Thermal Stability Engineering Using HoTMuSiC, in: Gáspári, Z. (Ed.), Structural Bioinformatics, Methods in Molecular Biology. Springer US, New York, NY, pp. 59–73. https://doi.org/10.1007/978-1-0716-0270-6_5

Pustake, M., Tambolkar, I., Giri, P., Gandhi, C., 2022. SARS, MERS and CoVID-19: An overview and comparison of clinical, laboratory and radiological features. J Family Med Prim Care 11, 10. https://doi.org/10.4103/jfmpc.jfmpc_839_21

Rack, J.G.M., Perina, D., Ahel, I., 2016. Macrodomains: Structure, Function, Evolution, and Catalytic Activities. Annu. Rev. Biochem. 85, 431–454. https://doi.org/10.1146/annurev-biochem-060815-014935

Rack, J.G.M., Zorzini, V., Zhu, Z., Schuller, M., Ahel, D., Ahel, I., 2020. Viral macrodomains: a structural and evolutionary assessment of the pharmacological potential. Open Biol. 10, 200237. https://doi.org/10.1098/rsob.200237

Robert, X., Gouet, P., 2014. Deciphering key features in protein structures with the new ENDscript server. Nucleic Acids Research 42, W320–W324. https://doi.org/10.1093/nar/gku316

Rodriguez-Vargas, J.M., Nguekeu-Zebaze, L., Dantzer, F., 2019. PARP3 comes to light as a prime target in cancer therapy. Cell Cycle 18, 1295–1301. https://doi.org/10.1080/15384101.2019.1617454

Rosenthal, F., Feijs, K.L.H., Frugier, E., Bonalli, M., Forst, A.H., Imhof, R., Winkler, H.C., Fischer, D., Caflisch, A., Hassa, P.O., Lüscher, B., Hottiger, M.O., 2013. Macrodomain-containing proteins are new mono-ADP-ribosylhydrolases. Nat Struct Mol Biol 20, 502–507. https://doi.org/10.1038/nsmb.2521

Roy, A., Alhammad, Y.M., McDonald, P., Johnson, D.K., Zhuo, J., Wazir, S., Ferraris, D., Lehtiö, L., Leung, A.K.L., Fehr, A.R., 2022. Discovery of compounds that inhibit SARS-CoV-2 Mac1-ADP-ribose binding by high-throughput screening. Antiviral Research 203, 105344. https://doi.org/10.1016/j.antiviral.2022.105344

Russo, L.C., Tomasin, R., Matos, I.A., Manucci, A.C., Sowa, S.T., Dale, K., Caldecott, K.W., Lehtiö, L., Schechtman, D., Meotti, F.C., Bruni-Cardoso, A., Hoch, N.C., 2021. The SARS-CoV-2 Nsp3 macrodomain reverses PARP9/DTX3L-dependent ADP-ribosylation induced by interferon signaling. Journal of Biological Chemistry 297, 101041. https://doi.org/10.1016/j.jbc.2021.101041

Schneider, C.A., Rasband, W.S., Eliceiri, K.W., 2012. NIH Image to ImageJ: 25 years of image analysis. Nat Methods 9, 671–675. https://doi.org/10.1038/nmeth.2089

Schuller, M., Correy, G.J., Gahbauer, S., Fearon, D., Wu, T., Díaz, R.E., Young, I.D., Carvalho Martins, L., Smith, D.H., Schulze-Gahmen, U., Owens, T.W., Deshpande, I., Merz, G.E., Thwin, A.C., Biel, J.T., Peters, J.K., Moritz, M., Herrera, N., Kratochvil, H.T., QCRG Structural Biology Consortium, Aimon, A., Bennett, J.M., Brandao Neto, J., Cohen, A.E., Dias, A., Douangamath, A., Dunnett, L., Fedorov, O., Ferla, M.P., Fuchs, M.R., Gorrie-Stone, T.J., Holton, J.M., Johnson, M.G., Krojer, T., Meigs, G., Powell, A.J., Rack, J.G.M., Rangel, V.L., Russi, S., Skyner, R.E., Smith, C.A., Soares, A.S., Wierman, J.L., Zhu, K., O'Brien, P., Jura, N., Ashworth, A., Irwin, J.J., Thompson, M.C., Gestwicki, J.E., von Delft, F., Shoichet, B.K., Fraser, J.S., Ahel, I., 2021. Fragment binding to the Nsp3 macrodomain of SARS-CoV-2 identified through crystallographic screening and computational docking. Sci. Adv. 7, eabf8711. https://doi.org/10.1126/sciadv.abf8711

Tan, J., Vonrhein, C., Smart, O.S., Bricogne, G., Bollati, M., Kusov, Y., Hansen, G., Mesters, J.R., Schmidt, C.L., Hilgenfeld, R., 2009. The SARS-Unique Domain (SUD) of SARS Coronavirus Contains Two Macrodomains That Bind G-Quadruplexes. PLoS Pathog 5, e1000428. https://doi.org/10.1371/journal.ppat.1000428

Tsika, A.C., Gallo, A., Fourkiotis, N.K., Argyriou, A.I., Sreeramulu, S., Löhr, F., Rogov, V.V., Richter, C., Linhard, V., Gande, S.L., Altincekic, N., Krishnathas, R., Elamri, I., Schwalbe, H., Wollenhaupt, J., Weiss, M.S., Spyroulias, G.A., 2022. Binding Adaptation of GS-441524 Diversifies Macro Domains and Downregulates SARS-CoV-2 de-MARylation Capacity. Journal of Molecular Biology 434, 167720. https://doi.org/10.1016/j.jmb.2022.167720

Voth, L.S., O'Connor, J.J., Kerr, C.M., Doerger, E., Schwarting, N., Sperstad, P., Johnson, D.K., Fehr, A.R., 2021. Unique Mutations in the Murine Hepatitis Virus Macrodomain

Differentially Attenuate Virus Replication, Indicating Multiple Roles for the Macrodomain in Coronavirus Replication. J Virol 95, e00766-21. https://doi.org/10.1128/JVI.00766-21

Wang, Y., Tang, Q., Maul, G.G., Yuan, Y., 2006. Kaposi's Sarcoma-Associated Herpesvirus *ori-Lyt* -Dependent DNA Replication: DualRole of Replication and Transcription Activator. J Virol 80, 12171–12186. https://doi.org/10.1128/JVI.00990-06

Wu, F., Zhao, S., Yu, B., Chen, Y.-M., Wang, W., Song, Z.-G., Hu, Y., Tao, Z.-W., Tian, J.-H., Pei, Y.-Y., Yuan, M.-L., Zhang, Y.-L., Dai, F.-H., Liu, Y., Wang, Q.-M., Zheng, J.-J., Xu, L., Holmes, E.C., Zhang, Y.-Z., 2020. A new coronavirus associated with human respiratory disease in China. Nature 579, 265–269. https://doi.org/10.1038/s41586-020-2008-3

Zhang, W., Wang, C., Song, Y., Shao, C., Zhang, X., Zang, J., 2015. Structural insights into the mechanism of Escherichia coli YmdB: A 2′- O -acetyl-ADP-ribose deacetylase. Journal of Structural Biology 192, 478–486. https://doi.org/10.1016/j.jsb.2015.10.010

Zhu, H., Tang, Y.-D., Zhan, G., Su, C., Zheng, C., 2021. The Critical Role of PARPs in Regulating Innate Immune Responses. Front. Immunol. 12, 712556. https://doi.org/10.3389/fimmu.2021.712556

Zhu, H., Zheng, C., 2021. When PARPs Meet Antiviral Innate Immunity. Trends in Microbiology 29, 776–778. https://doi.org/10.1016/j.tim.2021.01.002

Fig 1.

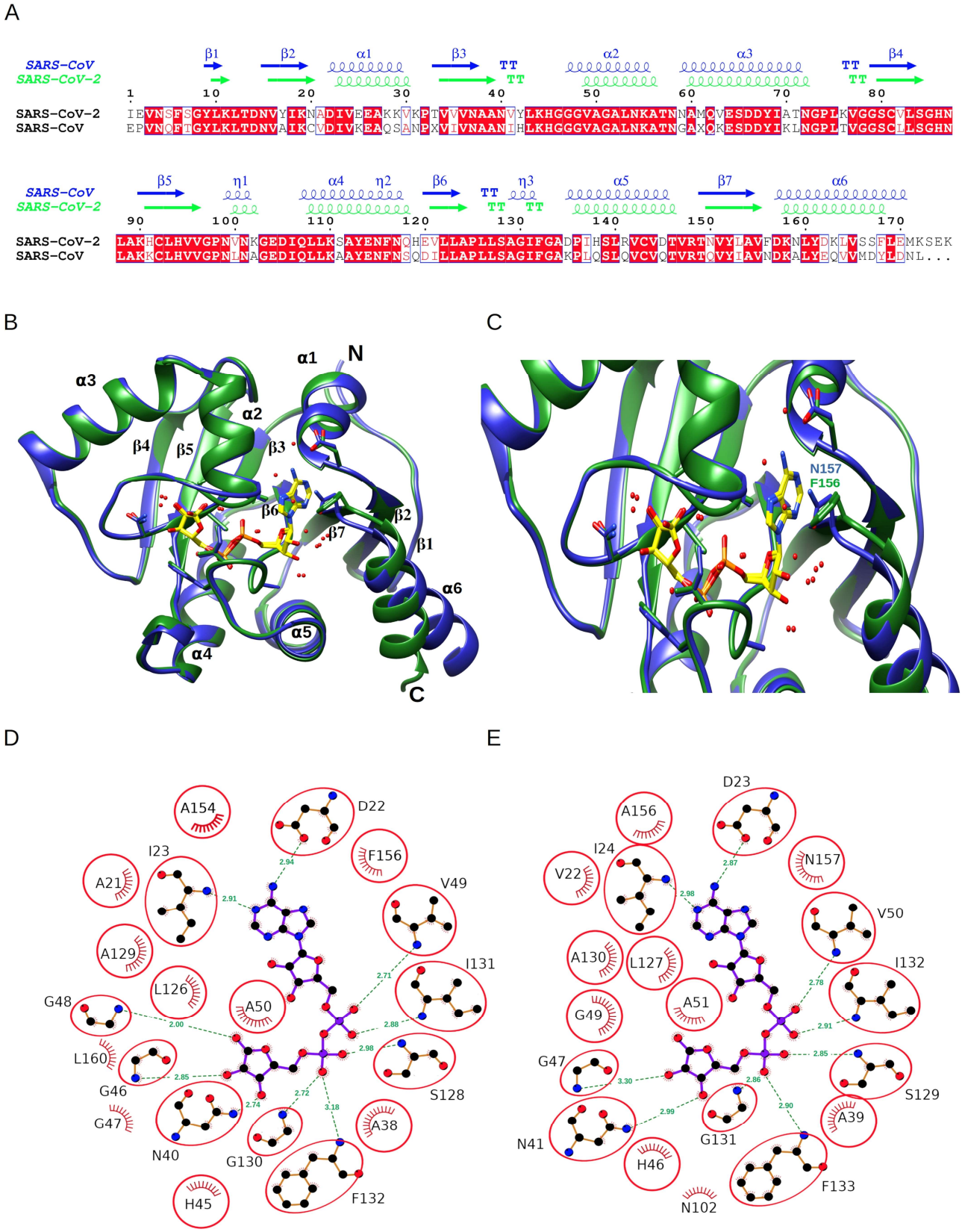
A
SARS-CoV
SARS-CoV-2
SARS-CoV-2
SARS-CoV
B
C
N
C
N157
F156
D
E
A154
D22
I23
F156
A21
V49
A129
I131
L126
A50
G48
S128
L160
G46
G47
N40
G130
A38
H45
F132
D23
A156
I24
N157
V22
V50
A130
L127
I132
A51
G49
G47
S129
A39
N41
G131
H46
F133
N102

Fig 2.

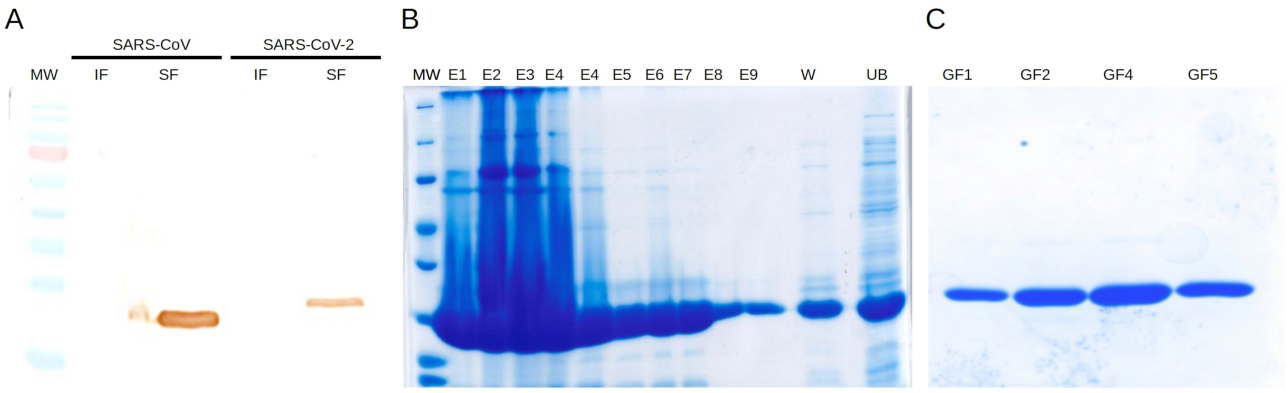
A
SARS-CoV
SARS-CoV-2
MW
IF
SF
IF
SF
B
MW E1 E2 E3 E4 E4 E5 E6 E7 E8 E9 W UB
C
GF1 GF2 GF4 GF5

Fig 3.

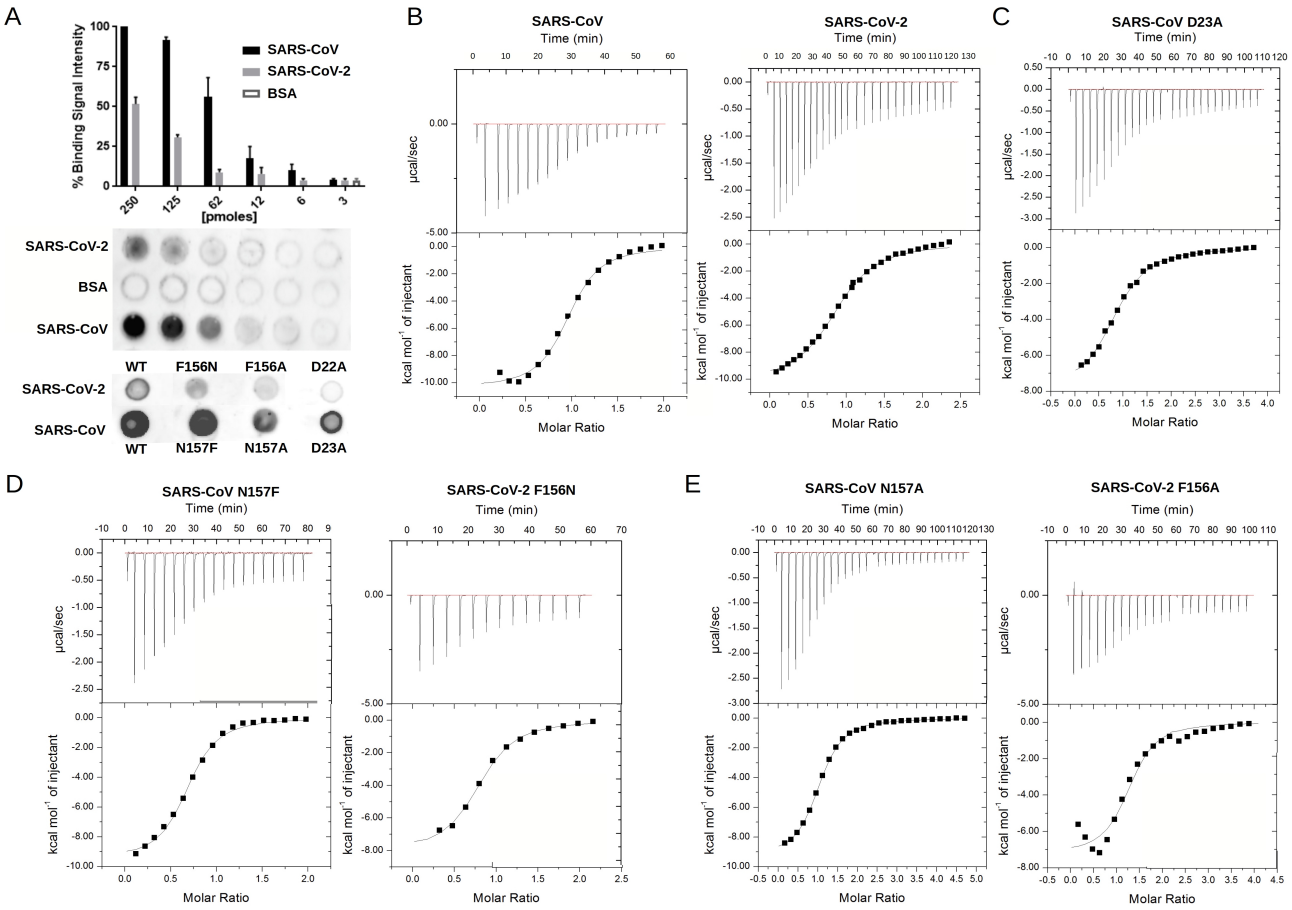
A
% Binding Signal Intensity
SARS-CoV
SARS-CoV-2
BSA
[pmoles]
SARS-CoV-2
BSA
SARS-CoV
WT
F156N
F156A
D22A
SARS-CoV-2
SARS-CoV
WT
N157F
N157A
D23A
B
SARS-CoV
Time (min)
SARS-CoV-2
Time (min)
µcal/sec
kcal mol-1 of injectant
Molar Ratio
C
SARS-CoV D23A
Time (min)
D
SARS-CoV N157F
Time (min)
SARS-CoV-2 F156N
Time (min)
E
SARS-CoV N157A
Time (min)
SARS-CoV-2 F156A
Time (min)

Fig 4.

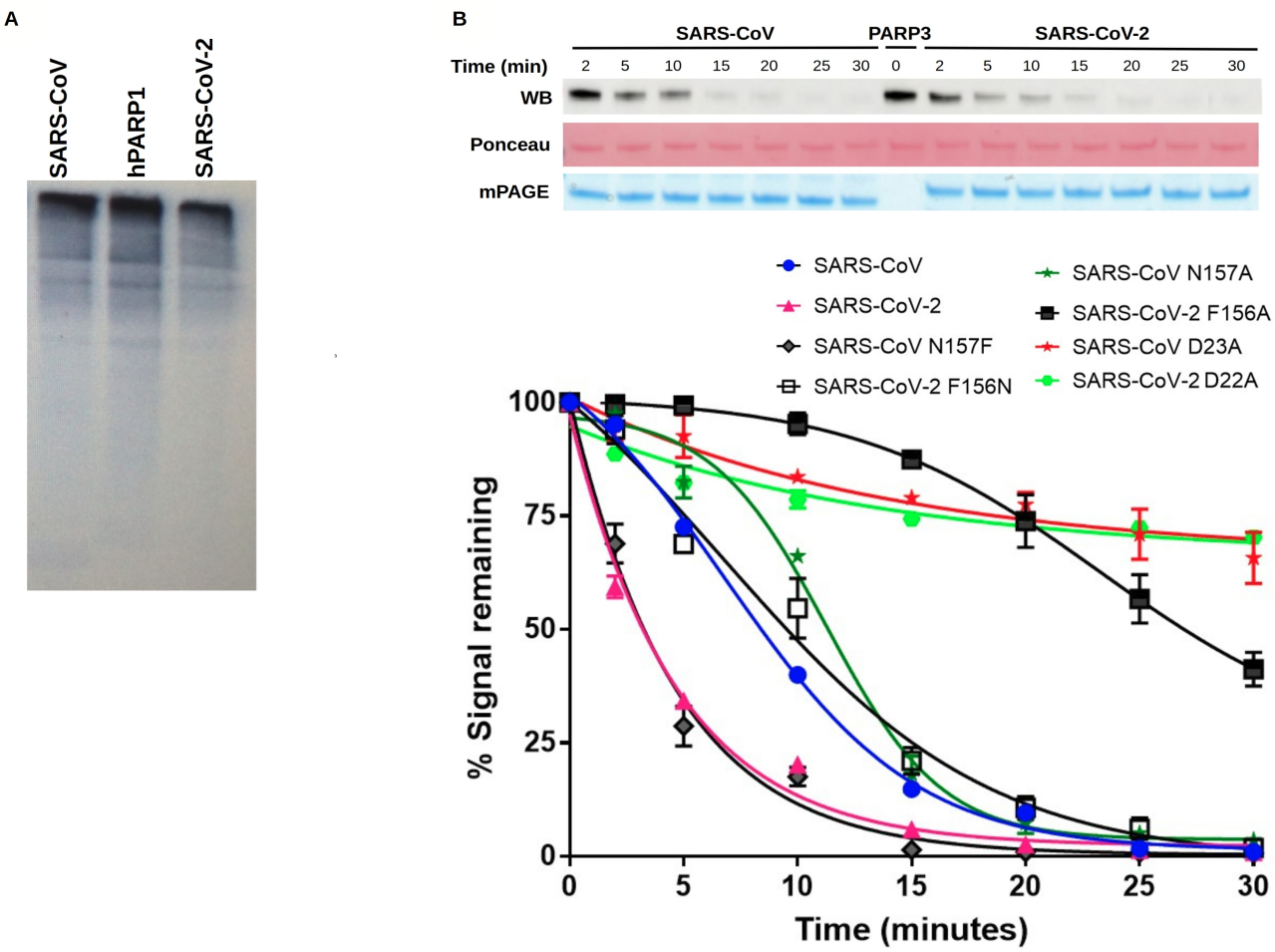
A
SARS-CoV
hPARP1
SARS-CoV-2
B
SARS-CoV
PARP3
SARS-CoV-2
Time (min)
2 5 10 15 20 25 30 0 2 5 10 15 20 25 30
WB
Ponceau
mPAGE
SARS-CoV
SARS-CoV-2
SARS-CoV N157F
SARS-CoV-2 F156N
SARS-CoV N157A
SARS-CoV-2 F156A
SARS-CoV D23A
SARS-CoV-2 D22A
% Signal remaining
100
75
50
25
0
0 5 10 15 20 25 30
Time (minutes)

Fig 5.

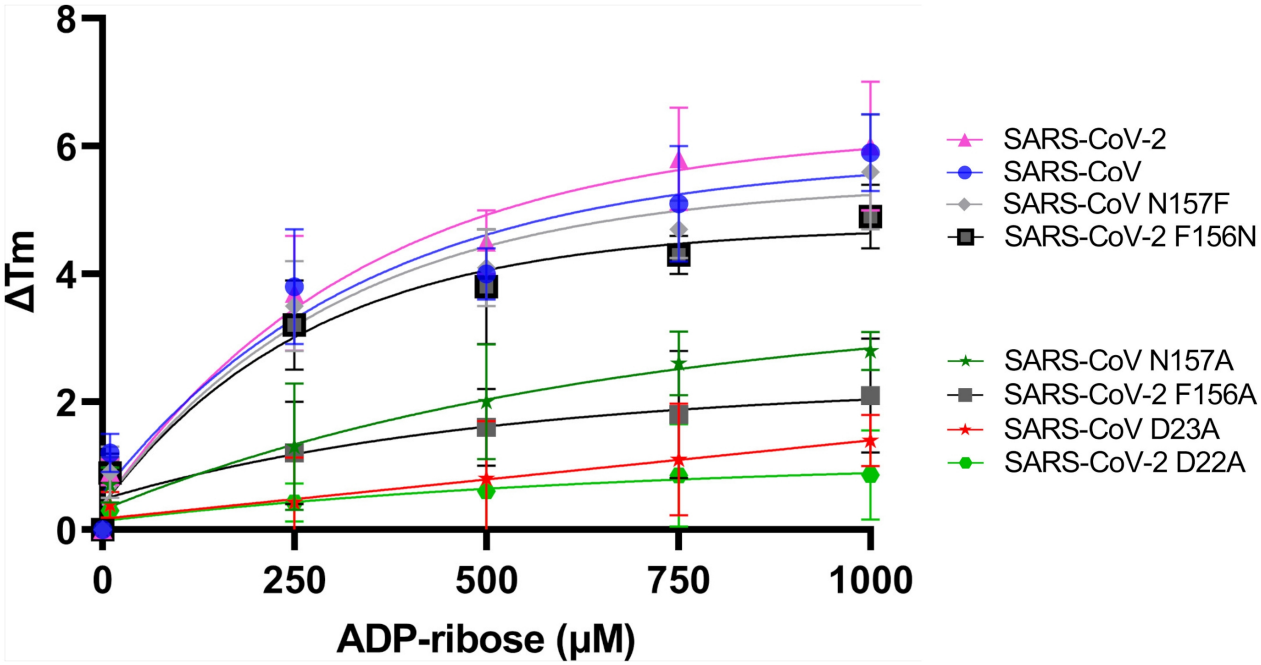
8
6
4
2
0
ΔTm
0
250
500
750
1000
ADP-ribose (μM)
SARS-CoV-2
SARS-CoV
SARS-CoV N157F
SARS-CoV-2 F156N
SARS-CoV N157A
SARS-CoV-2 F156A
SARS-CoV D23A
SARS-CoV-2 D22A

Supplementary materials

Table S1. Primers template of CoV *Macro1* domains mutants.

CoV *Macro1* domain mutants	Forward Primer Sequence (5' to 3')	Reverse Primer Sequence (5' to 3')
SARS-CoV-N157F	5'-ACCCAGGTTTACATCGCGGTGTTCGATAA-3'	5'-AACCTGTTCGTACAGGGCTTTATCGAACACCG-3'
SARS-CoV-2 F156N	5'-GTACCAACGTGTACCTGGCGGTGAATGATAA-3'	5'-CTGGAGACTAATTTGTCATACAAATTTTTATCATTCACCG-3'
SARS-CoV N157A	5-ACCCAGGTTTACATCGCGGTGGCCGATAA-3'	5'-AACCTGTTCGTACAGGGCTTTATCGGCCACCG-3'
SARS-CoV-2 F156A	5'-GTACCAACGTGTACCTGGCGGTGGCTGATAA-3'	5-'CTGGAGACTAATTTGTCATACAAATTTTTATCAGCCACCG-3'
SARS-CoV D23A	5'-GATAATGTCGCCATTAAGTGCGTAGCTATTGTG-3'	5'-CACT-CTGTGCTTCTTTCACAATAGCTACGC-3'
SARS-CoV-2 D22A	5'-CAATGTGTACATTAAAAATGCGGCCATTGTTG-3'	5'-CCTTTTTTGCTTCTTCAACAATGGCCGCATT-3'

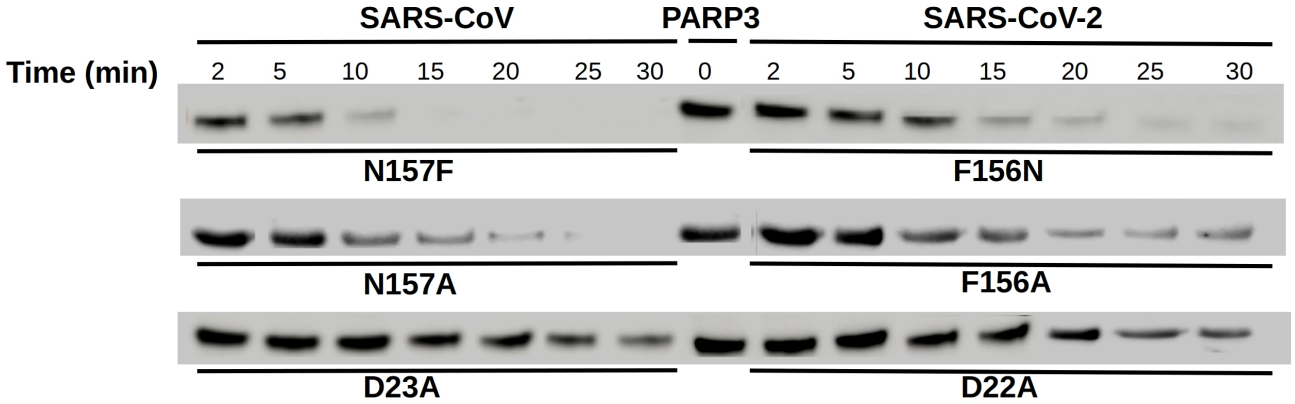

Figure S1. de-MARylation activity by CoV *Macro1* domains mutants. Western blot of auto-MARylated hPARP3 with SARS-CoV and SARS-CoV-2 *Macro1* domains mutants.